

Research Article

Electrolytic Manganese Residue-Modified Asphalt Performance Test and Micromechanism Analysis

Tao Fu ¹, Bin Pang,² Haoxu Li ¹, Junlin Liang ¹ and Huiming Bao ³

¹College of Civil Engineering and Architecture, Guangxi University, Nanning 530004, China

²The Road and Bridge Engineering Department of Guangxi Vocational and Technical College of Communications, Nanning 530004, China

³College of Civil Engineering and Architecture, Guilin University of Technology, Guilin 541004, China

Correspondence should be addressed to Junlin Liang; ljl_1217@126.com and Huiming Bao; bhming@163.com

Received 18 May 2020; Revised 18 July 2020; Accepted 10 August 2020; Published 20 August 2020

Guest Editor: Meng Guo

Copyright © 2020 Tao Fu et al. This is an open access article distributed under the Creative Commons Attribution License, which permits unrestricted use, distribution, and reproduction in any medium, provided the original work is properly cited.

The aim of this paper is to study the feasibility of using an electrolytic manganese residue (EMR) as modified asphalt. In this paper, after grinding the electrolytic manganese residue (EMR) into asphalt, the electrolytic manganese residue- (EMR-) modified asphalt was prepared with different mix ratios. The three major indicators of the modified asphalt were studied, and its modification mechanism was studied by differential scanning calorimetry, infrared spectroscopy, and atomic force microscopy. The adhesion force, surface energy, and dissipation energy of the asphalt before and after modification were analyzed by a force curve. The results show that the surface energy of the electrolytic manganese residue (EMR) is increased after grinding, the high temperature performance of the asphalt is improved, and the temperature sensitivity of the asphalt is decreased; however, the low-temperature performance is not improved obviously. When the powder oil ratio is 9%, the comprehensive performance of the asphalt is the best. The results of the infrared spectrum analysis show that the mixture of the electrolytic manganese residue (EMR) and asphalt does not produce new functional groups, and thus, the preparation method is a physical modification method. The differential scanning calorimetry (DSC) results show that the electrolytic manganese residue (EMR) can enhance the high-temperature stability of asphalt. It is found that the stability and antideformation ability of the modified asphalt improved.

1. Introduction

Manganese is widely used in steel, nonferrous alloys, battery materials, the chemical industry, and agriculture [1–4]. China is the world's leading producer of manganese. Manganese products mainly include electrolytic metal manganese, electrolytic manganese dioxide, manganese ferroalloy, and manganese ore. In 2018, China's production capacity of electrolytic manganese residue (EMR) was 2.26 million tons, and the actual output was 1.4 million tons, accounting for 97% of the total output of the production capacity of electrolytic manganese in the world. Electrolytic manganese residue (EMR) is acid leaching slag produced in the process of electrolyte preparation, and it is the key pollutant generated by the electrolytic manganese industry. The grade of manganese ore in China is relatively low, and

8–10 tons of electrolytic manganese residues (EMRs) will be produced for every 1 ton of manganese produced. At present, the amount of electrolytic manganese residue (EMR) in China has exceeded 100 million tons, with an annual increase of more than 10 million tons. Electrolytic manganese residue (EMR) also has the characteristics of a high moisture content (22%~28%), fine particles (up to 70% of particles have sizes <30 μm), a high sulfate content (20%~30%, as calculated by SO_3), and good thermal stability. The apparent density is 2039 kg/m^3 , and the packing density of wet slag and dry slag is 1785 kg/m^3 and 1982 kg/m^3 , respectively. By improving the technology level of a harmless treatment and utilizing electrolytic manganese residue (EMR), reducing the storage and risk of electrolytic manganese residue (EMR) by scientific and reasonable means is being widely studied [5–8]. Therefore, the effective

utilization of electrolytic manganese residue (EMR) resources can not only produce good environmental and social benefits but also bring good economic benefits to electrolytic manganese residue (EMR) plants [9–11].

At present, many studies have been carried out on the utilization of electrolytic manganese residue (EMR). Wang et al. [10] aimed to prepare nonsintered permeable bricks with a large amount of electrolytic manganese residue (EMR), which is discharged from the electrolytic manganese industry as raw materials. The mechanical properties and environmental properties are studied so that EMR can be successfully applied to pavement materials. Tang's articles [9] also presented relevant research. Zhang et al. [12] studied the chemical composition, mechanical properties, hydration behavior, pore structure, and environmentally friendly properties of materials prepared with different calcium silicon ratios by using EMR and red mud as road base materials. The research results provide a direction for the large-scale and effective utilization of electrolytic manganese residue (EMR). Hou et al. [13] prepared Q-SACs by adding different amounts of electrolytic manganese residue (EMR) (10–45%) to study the chemical composition, basicity, setting time, and compressive strength of the mineral. The results show that the Q-SACs with electrolytic manganese residue (EMR) have a good strength, a low firing temperature, and good mechanical properties. Qin et al. [14] discussed the influence of electrolytic manganese slag on the road performance of an asphalt mixture. The results show that the high-temperature stability performance and corrosion resistance began to significantly increase by adding electrolytic manganese residue (EMR).

The objective of this study was to investigate electrolytic manganese residue- (EMR-) modified asphalt. Additionally, penetration tests, ductility tests, and softening point tests are important tests for future research and practical applications. Otherwise, XRD, IR, DSC, and AFM testing methods are applied to discuss the properties of the EMR-modified asphalt.

2. Experimental Design

2.1. Materials

2.1.1. EMR. In the test, the EMR is the water-quenched slag obtained from the ferromanganese blast furnace of the Bayi ferroalloy plant in Laibin, Guangxi. The EMR contains gray-green loose particles with an average particle size of ≤ 3 mm and has a density of approximately 2.89 g/cm^3 and a loose bulk density of approximately 723 kg/m^3 . The chemical composition of the EMR is shown in Table 1.

The original EMR particles are grounded by a high-energy ball mill. After grinding for 25 min and 50 min, the diffraction analysis is carried out on the ground EMR by a Panak X'Pert Pro diffractometer in the Netherlands. The results are shown in Figure 1. In Figure 1(a), the peak intensity of the SiO_2 diffraction peak obtained for the powder after grinding for 25 min is 630 a.u.; in Figure 1(b), the peak intensity of the SiO_2 diffraction peak obtained for the powder after grinding for 50 min is 496 a.u. With the

TABLE 1: The main components of EMR (%).

SiO_2	Al_2O_3	CaO	MgO	Fe_2O_3	SO_3	MnO	Loss
23.86	16.32	37.81	6.52	1.23	0.48	9.60	0.72

increase in the mechanical grinding time, the intensity of the SiO_2 diffraction peak obtained for the powder decreases, the crystallinity of the crystal decreases, and amorphous substances are produced at the same time. The activity of the EMR increases with the increase in the grinding time.

According to molecular dynamics and the dispersion theory [15], the smaller the particle size is, the larger the specific surface area of the EMR is and the larger the contact area with asphalt is; the longer the grinding time of the EMR is, the smaller the particle size is and the smaller the crystallinity is, thus enhancing the activity. The smaller the particle size is, the more uniform the distribution is and the more stable the blending performance with asphalt is. Therefore, the particle size is approximately $35 \mu\text{m}$ after ball milling for 50 min, and the EMR is mixed with an asphalt matrix.

2.1.2. Asphalt Matrix. The matrix asphalt used in this experiment is the "Donghai brand" 70# road petroleum asphalt produced by Maoming Branch of Sinopec. The corresponding technical indicators of the matrix asphalt are in strict accordance with the technical requirements of the road petroleum asphalt (JTG F40-2004) standard. The penetration, softening point, and ductility indicators of the asphalt matrix are shown in Table 2.

2.2. Test Method

2.2.1. Physical Property Test. The major physical properties of asphalt, including penetration (temperature susceptibility, ASTM D5), softening point (high-temperature properties, ASTM D36), and ductility (low-temperature properties, ASTM D2801-95), were tested.

2.2.2. Differential Scanning Calorimetry. A DSC spectrometer (Zetseh DSC204), which was produced in Germany, was used to determine the functional characteristics of asphalt in the experiment, in which the asphalt was heated at a rate of $10^\circ\text{C}/\text{min}$, and the nitrogen flow rate was $30 \text{ ml}/\text{min}$. The starting temperature was -10°C , and the ending temperature was 200°C .

2.2.3. Atomic Force Microscopy. AFM (Bruke Dimension ICON) was used to test the MA, RMMA, and RMMAFC. In the AFM experiment, a tiny and spiky tip (length: $125 \mu\text{m}$; natural frequency: 70 kHz ; spring constant: 3 N/m) was attached at the unsupported end of the cantilever and remained close to the asphalt film. Due to the close contact between the tips and the surface of the film, a repulsive or attractive force between the atoms of the top layer of asphalt and the AFM tip is created, which deflects the cantilever. The extent of the deflection absolutely depends on the force developed between the molecules of the tips and the film.

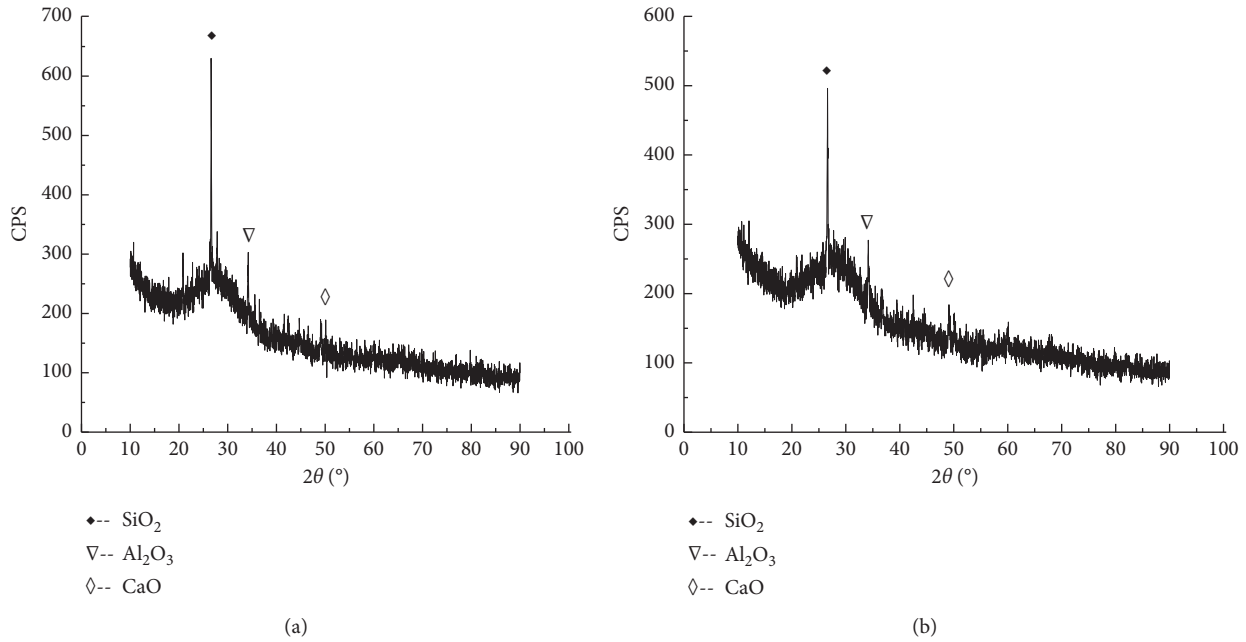


FIGURE 1: XRD patterns of the EMR after different grinding times. (a) 25 min. (b) 50 min.

TABLE 2: Basic properties of the matrix asphalt.

Test project	Test results		Industry standard
	Value	Unit	
Penetration (25°C)	64.2	0.1 mm	60–80
Ductility (15°C)	105.2	cm	≥ 100
Softening point	48.1	°C	≥ 46
Solubility	99.73	%	≥ 99.5
Flash point	298	°C	≥ 260

2.2.4. Fourier Transform Infrared Spectroscopy. The instrument used in the FTIR experiment is a Nicote 7T40FTIR Fourier transform infrared spectrometer (made in the United States), which was used to determine the functional characteristics of asphalt, and data was collected for the wavenumber range of $400\text{--}4000\text{ cm}^{-1}$.

2.3. Preparation of EMR Asphalt. The EMR milled for 50 min was dried to a constant mass at 105°C . An appropriate amount of asphalt was obtained and melted to the flowing state in an oven at 135°C . The modified asphalt was prepared by a high-speed shear dispersion emulsifier and heated at $160\text{--}170^\circ\text{C}$ for 30 min, and the asphalt was prepared with a powder:oil ratio of 0%, 3%, 6%, 9%, 12%, and 15%.

3. Results and Discussion

3.1. Performance Test of the EMR Asphalt Mortar

3.1.1. Penetration Test. The penetration test was carried out at a series of temperatures (10°C , 15°C , 20°C , 25°C , and 30°C). The needle penetration value is shown in Table 3. With the increase in the powder oil ratio, the needle penetration value at high temperatures decreases continuously, but the change

is not obvious at low temperatures. When the powder:oil ratio reaches 9%, the decrease in the amplitude of the high temperature value is larger than that obtained for the other powder:oil ratios, and then, the effect of increasing the powder:oil ratio on the needle penetration value is not obvious. The penetration index PI, the equivalent softening point T_{800} , the equivalent brittle point $T_{1,2}$, and the plastic temperature range ΔT are calculated by linear regression of the one-dimensional first-order equation, which was combined with the penetration values for a series of temperatures. The penetration index PI reflects the degree of penetration changing with temperature. The higher the PI, the lower the temperature sensitivity of asphalt. As shown in the table, when the PI value of the asphalt matrix is -0.9 and when the powder:oil ratio of the EMR micropowder asphalt reaches 9%, the PI first shows a peak value of -0.769 ; then, when the powder:oil ratio reaches 15%, the PI value again shows a peak value of -0.741 and continues to increase the powder:oil ratio, but the PI value decreases. It can be seen that when the powder:oil ratio is 15%, the temperature sensitivity of the asphalt is lower than that of the asphalt prepared with the other powder:oil ratios. The equivalent softening point T_{800} reflects the high-temperature performance of asphalt. When the powder:oil ratio is 9%, the T_{800} reaches the peak value of 51.1°C , which is approximately 2°C higher than that of the asphalt matrix at 49.4°C , and then slightly decreases. When the powder:oil ratio is 15%, the peak value of 51.3°C appears again. The equivalent brittle point $T_{1,2}$ reflects the low-temperature crack resistance of asphalt. $T_{1,2}$ first increased with the increase in the powder:oil ratio and then decreased to -11.8°C when the powder:oil ratio was 9%. The plastic temperature range ΔT represents the difference between T_{800} and $T_{1,2}$. The larger the temperature range is, the wider the temperature range is. ΔT first

TABLE 3: Summary table of the test results of three indicators.

R	Penetration test						Ductility				SP		
	Penetration of different temperatures (0.1 mm)					PI	T_{800}	$T_{1.2}$	ΔT	1 cm/m in 5°C		5 cm/m in 15°C	°C
	10°C	15°C	20°C	25°C	30°C					cm		cm	
0	12.3	21.1	32.6	61.2	102.5	-0.92	49.40	-11.80	61.25	100.0	150.0	49.2	
3	11.8	21.0	32.5	61.0	101.0	-0.99	49.29	-11.36	60.65	98.0	150.0	52.3	
6	11.5	19.8	32.2	57.8	98.8	-1.00	49.54	-11.97	60.51	97.0	150.0	56.2	
9	11.6	18.8	31.3	52.8	92.3	-0.77	51.08	-11.67	62.75	90.0	141.6	57.9	
12	11.4	19.7	29.9	53.7	91.6	-0.81	50.85	-11.50	62.35	86.0	139.1	57.5	
15	11.3	19.7	30.6	53.7	90.2	-0.74	51.23	-11.79	63.03	84.0	97.3	54.5	
18	11.2	17.3	31.9	53.6	90.2	-0.90	50.55	-10.89	61.44	74.0	78.2	52.3	
21	11.4	18.7	32.2	52.3	89.9	-0.74	51.27	-11.75	63.02	59.0	65.6	50.1	

decreased and then increased with the addition of EMR, reaching the peak value when the powder:oil ratio was 9%, and then, ΔT reached the peak value again when the powder:oil ratio was 15%. The comprehensive analysis shows that the addition of EMR can improve the penetration resistance to a certain extent and can improve the high-temperature mechanical properties of asphalt; the best content is a 9% powder:oil ratio, but this ratio has no obvious effect on the low-temperature crack resistance of asphalt

3.1.2. Ductility Test. The ductility reflects the extension length of asphalt at a specific temperature and tensile rate and reflects the pavement performance and low-temperature crack resistance. When the powder:oil ratio is less than or equal to 6%, the ductility of the modified asphalt and asphalt matrix is 150 cm. With the increase in the powder:oil ratio, the ductility of asphalt decreased; when the powder:oil ratio reached 15%, the ductility decreased to 87.3 cm. The results show that, with the addition of the inorganic EMR to the organic colloidal material asphalt, a whole blended structure is formed; however with the increase in the ratio of powder to oil, too much EMR lacks enough asphalt colloid to generate adhesion, so the ductility value under the external tensile action is lower than that of the original asphalt matrix.

3.1.3. Softening Point Test. The softening point reflects the high-temperature deformation resistance of asphalt. With the addition of EMR, the softening point of asphalt increased. When the powder:oil ratio is 9%, the softening point reaches the peak value of 57.9°C, which is 5.6°C higher than that of 52.3°C when the powder oil ratio is 3%; then, when the powder:oil ratio is increased, the temperature of the softening point decreases close to the performance of the matrix asphalt. The results show that the addition of EMR can reduce the temperature sensitivity of asphalt and improve its high temperature stability, which shows that the softening point temperature of asphalt increases.

3.2. Infrared Spectrum Analysis. A Thermo Nexus 470 FT-IR spectrometer was used to test the EMR and asphalt. The test range was 400–4000 cm^{-1} , and the test was repeated 5 times.

As shown in Figure 2, the peak at 1029 cm^{-1} in the spectrum of the EMR is the vibration absorption peak of Si-O in the EMR, and the peak at 468 cm^{-1} is the absorption band position of the alumina-like oxide in the corundum structure; the peaks are 2923 cm^{-1} and 2852 cm^{-1} in the spectrum of the matrix asphalt are the C-H (CH_3 -, $-\text{CH}_2$ -) stretching vibration bands of asphalt, the peaks at 1460 cm^{-1} and 1376 cm^{-1} are the C-H bending vibration bands of asphalt, and the peak at 1602 cm^{-1} is the stretching vibration band of the carbonyl (C=O) group in asphalt; the spectrum of the asphalt with a 6% powder:oil ratio is basically the same as that of the matrix asphalt, and only the stretching vibration band of the carbonyl (C=O) group shifts to 1608 cm^{-1} ; in the spectrum of the asphalt with a 9% powder:oil ratio, the stretching vibration band of C-H shifts to 2921 cm^{-1} and 2851 cm^{-1} , that is to say, it moves toward the low-frequency direction, and the bending vibration band shifts to 1455 cm^{-1} and 1382 cm^{-1} , moving toward the high-frequency region. According to the change in the functional group position in Figure 2 and the factors affecting the band position, it is found that the atoms of N, P, and S in the EMR form hydrogen bonds with the atoms of asphalt that do not shared electron pairs, but the polarity of the hydrogen bond that formed is also weak due to the weak polarity of the atoms of N, P, and S; the stretching vibration frequency of the weak hydrogen bond of the original bond will move toward the low-frequency direction, and the displacement is small. Meanwhile, the bending vibration of asphalt will move toward the high-frequency region, and the band is narrow, which will increase the activity of asphalt. The penetration and softening point performance indexes of asphalt are related to the relative proportion of high and low molecular weight hydrocarbons in the asphalt. After the EMR is added to the asphalt during modification, the Al_2O_3 absorption band does not appear in the spectra obtained for the asphalt with 6% and 9% powder:oil ratios. According to the catalytic oxidation mechanism of petroleum asphalt, Al_2O_3 adsorbs the small and medium molecular weight components of the aliphatic hydrocarbons and aromatic hydrocarbons under high temperature conditions for oxidation. In the cross-linking and condensation reaction, when the high molecular weight increases, the unreacted part of Al_2O_3 will be

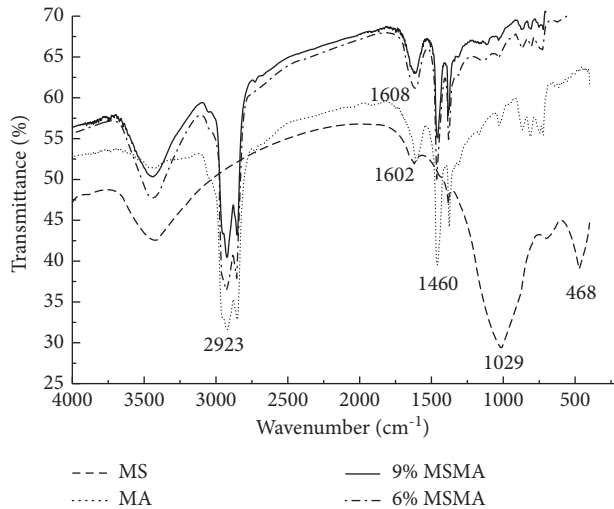


FIGURE 2: Infrared spectra of the EMR and asphalt.

replaced by a low molecular weight component and will continue to play the role of the catalytic oxidant so that the content of the high molecular weight hydrocarbon in the asphalt will increase. In addition, the distribution of the penetration value and penetration index PI will appear as a hump with the increase in the powder:oil ratio, which is consistent with the other results. In addition, as shown in the spectra of the asphalt with a 9% powder:oil ratio, the carbonyl group of the asphalt will be replaced. The shift in the (C=O) stretching vibration band to 1621 cm^{-1} in the high-frequency direction also indicates that the oxidation of asphalt occurs after the addition of EMR; meanwhile, the intermolecular forces increase, and the polarity increases.

The uniformity of the distribution of the modifier has a great influence on the performance and stability of the asphalt. Because of the complexity of the chemical composition of EMR, a series of physical and chemical reactions may take place after the asphalt is mixed. For the dispersion of the inorganic modifier mixed with asphalt, according to the intensity of the infrared absorption peak at the wavenumber of a specific functional group in the infrared spectra, the literature characterizes the relative amount of the inorganic modifier and asphalt and describes the uniform and stable state of the inorganic modifier mixed with asphalt by comparing whether the relative amount of the two changes linearly as the amount of the modifier changes. In this paper, the infrared absorption strength at the wavenumber 1602 cm^{-1} (denoted as $H_{1602}\text{ cm}^{-1}$) is used to characterize the relative amount of EMR, and the infrared absorption strength at the wavenumber 1455 cm^{-1} (denoted as $H_{1455}\text{ cm}^{-1}$) is used to characterize the relative amount of asphalt. The ratio of the two is used to characterize the relative content of EMR and asphalt in the modified asphalt. The results are shown in Table 4 below. At wavenumber 1602 cm^{-1} , the infrared absorption strength of the EMR is 0.078; at 6%, the infrared absorption strength of the asphalt is 0.068, which is less than that of the EMR; at 9%, the infrared absorption strength of the asphalt is 0.083, which is greater than that of the EMR; these results are different from

those of other modifiers because of the catalytic oxidation of the Al_2O_3 component in EMR. When the content of Al_2O_3 is small, the crosslinking and condensation reaction occurring between Al_2O_3 and asphalt takes place first to generate high molecular weight hydrocarbon. As the content of Al_2O_3 continues to increase, the reaction continues to generate high molecular weight material, and the infrared absorption strength increases accordingly. In addition, the unreacted surplus Al_2O_3 is also replaced by low molecular weight components. Therefore, although the infrared absorption strength increases, it is close to the infrared absorption strength of EMR. In addition, the linear change in the absorption strength of the two shows that the EMR can be mixed evenly in asphalt, which proves that the addition of EMR can improve the performance of asphalt.

3.3. Differential Scanning Calorimetry. The asphalt matrix, asphalt with a 9% powder:oil ratio, and asphalt with a 12% powder:oil ratio were tested by a German DSC 204 differential scanning calorimeter, as shown in the DSC curve obtained for the asphalt samples with different powder:oil ratios in Figure 3.

The base peak area of the DSC curve corresponds to the thermal effect. The DSC curve of the asphalt is shown in Table 5. The energy value of the endothermic peak is characterized by the peak area of the DSC curve. Under the same test conditions, the endothermic peak area of the EMR micropowder series asphalt is lower than that of the asphalt matrix, which indicates that the matrix asphalt changes more than the EMR-modified asphalt in the range of test temperatures. According to the peak temperature of the endothermic peak, the thermal stability of the asphalt with the 9% powder:oil ratio is the best, which is approximately 49% higher than that of the matrix asphalt; the stability of the asphalt with a 12% powder:oil ratio is the second best and is still higher than that of the matrix asphalt. The peak temperature of the endothermic peak of the asphalt matrix increases by approximately 28%, which is consistent with the three major indexes of the EMR micropowder asphalt, the penetration index PI, equivalent softening point T_{800} , equivalent brittle point $T_{1,2}$, and plastic temperature range ΔT . The performance of the asphalt with the 9% powder:oil ratio is better than that of the asphalt with the 12% powder:oil ratio. The results show that the heat absorption of the asphalt decreases, the high-temperature stability of the asphalt is obviously improved, and the temperature sensitivity of the asphalt is significantly improved after the addition of the EMR micropowder during the DSC test used to study the performance degradation.

3.4. AFM Analysis

3.4.1. AFM Image Analysis. Two groups of experiments were carried out on the matrix asphalt (MA) and the 9% EMR-modified asphalt (MRMA). The two-dimensional and three-dimensional microscopic phase diagram of the asphalt under AFM is shown in Figures 4 and 5. Prabir named three parts with different morphologies as the continuous phase,

TABLE 4: Infrared absorption intensity at the wavenumbers 1602 cm⁻¹ and 1455 cm⁻¹.

Type	MA	6% MRMA	9% MRMA	MS
H1602 cm ⁻¹	—	0.068	0.083	0.078
H1455 cm ⁻¹	0.105	0.118	0.143	—
(H1602 cm ⁻¹)/(H1455 cm ⁻¹)	—	0.576	0.580	—

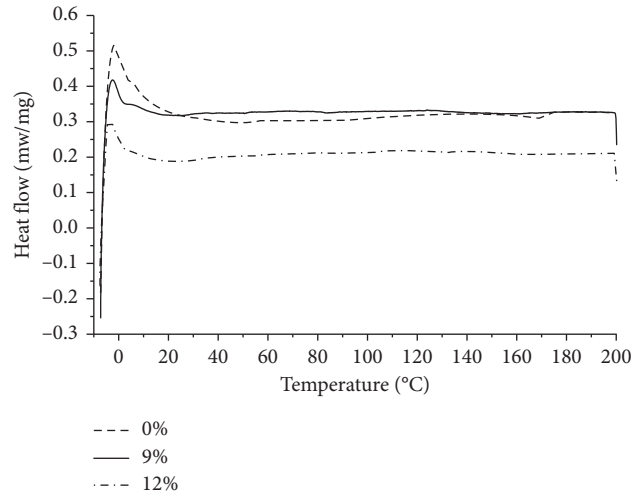


FIGURE 3: DSC curve of asphalt with different powder:oil ratios.

TABLE 5: DSC endothermic peak data of asphalt.

Type	Endothermic peak energy (J·g ⁻¹)	Peak temperature (°C)	Peak width (°C)
MA	666.47	-1.776	-7.241~200.706
9% MRMA	651.83	3.463	-0.537~199.463
12% MRMA	416.96	2.458	-0.542~199.458

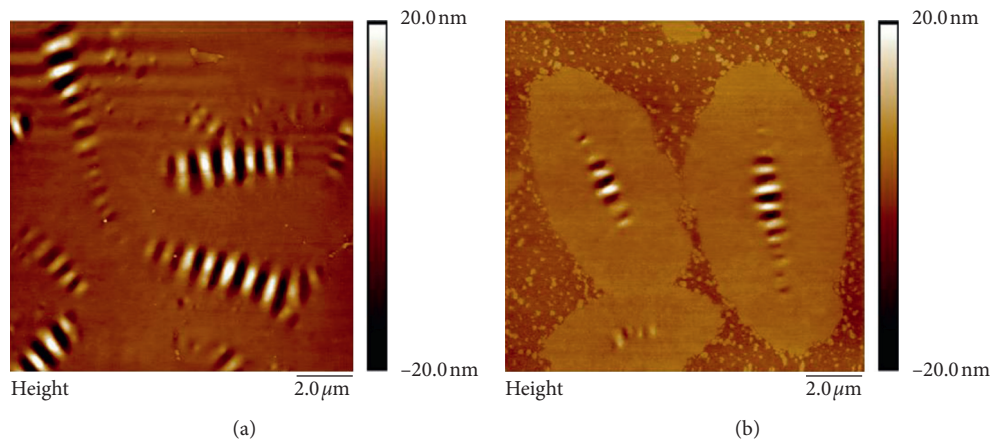


FIGURE 4: 2D AFM image of the (a) MRMA and (b) MA.

periphase, and bee phase. Image Pro Plus is used to process the image to highlight the contour of the bee structure; the bee structure was marked, and the area was counted, as

shown in Figure 6. The statistical results of the area are shown in Table 6. The results and causes are as follows:

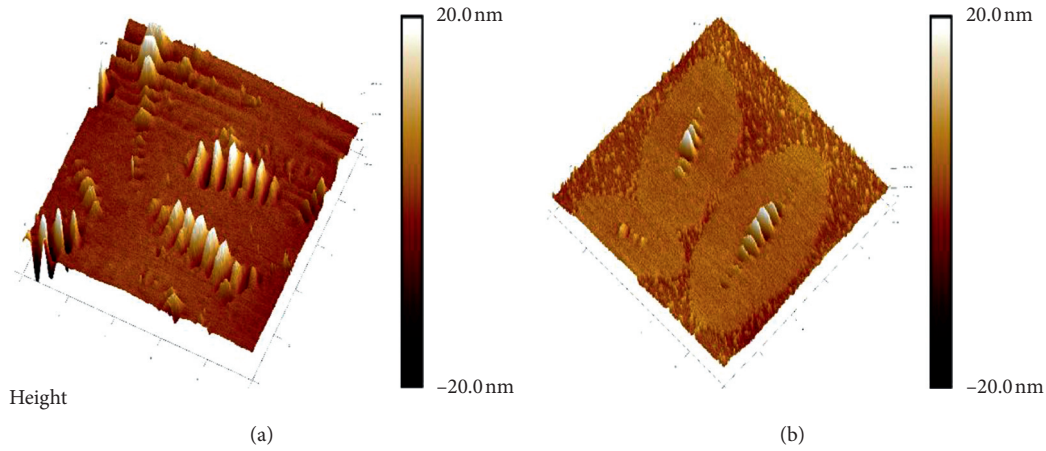


FIGURE 5: 3D AFM image of the (a) MRMA and (b) MA.

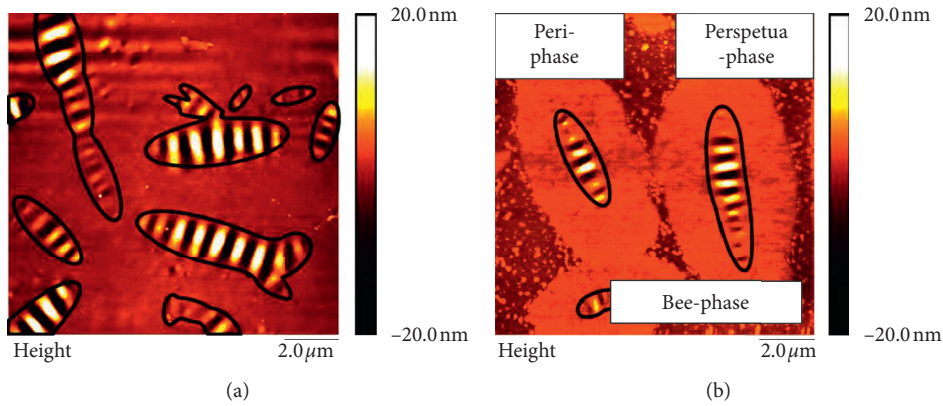


FIGURE 6: Bee structure. (a) MRMA and (b) MA.

TABLE 6: Matrix statistical table of the area of the bee-like structures.

Species of asphalt	Scanning range (μm^2)	Area			Maximal bee structure (μm^2)	Proportion of bee structure area (%)
		Continuous phase (μm^2)	Periphase (μm^2)	Bee-like structure (μm^2)		
MRMA	95.61	70.1	0	25.5	6.4	26.6
MA	95.61	37.5	50.2	7.9	4.6	8.3

(1) Before and after EMR modification, the microsurface of the asphalt has a bee structure. Under the influence of the EMR, the inclusion phase disappears, and the continuous phase is relatively flatter on the surface of the MRMA than it is on the surface of the MA; the number of bee structures increases significantly, the size of the bee structures increases, the difference between the sizes of the bee structures increases greatly, and some bee structure distortion and asphalt surface height differences are significant; there is a cross phenomenon between some of the bee structures, and the bee structures are still independent of each other. The bee structure accounts

for more than 24% of the total surface area, which is approximately 3 times the contribution of the MA bee structure. The honeycomb structure on the surface of the MA is rare, isolated, and regular in shape. With a three-phase morphology, obvious inclusions can be observed. The inclusions occupy 52.5% of the surface area of the MA, and the continuous phase is relatively rough, with many needle-like crystals densely distributed.

(2) The change in the bee-like structure of the MRMA showed that EMR could promote the formation and development of the bee-like structure. The asphaltene gum is wrapped by asphaltene to form micelles,

which are suspended in the oil; the chemical stability of the gum is poor, and it easily oxidizes and condenses into asphaltene. When the slurry is cooled, the wax components gather in the gum and asphaltene and grow up gradually by using the wax center as the core; when the content of asphaltene and gum in the slurry increases, the size of the wax nodule center increases at the same time, resulting in only small wax crystals. The surface acicular crystal of the MA is a wax crystal. The extremely polar colloid can wrap around the wax crystal and prevent the growth of the wax crystal. The reduction state of the EMR makes the resin oxidize and condense into asphaltene with a high molecular weight (1 000–100 000), and the wax with a low molecular weight (below 1000) decreases its saturation concentration during cooling. After the wax crystal is unbound, the amount of wax precipitates increases under the effect of cooling crystallization and temperature stress. As a result, the number of MRMA wasps increased. Some studies have shown that the texture of the inclusion phase is hard and that of the continuous phase is soft. Therefore, it is speculated that after the disappearance of the inclusion phase in the EMR; due to the lack of binding of the inclusion phase, the bee-shaped structure develops along the long and short axes, so the size of the bee-shaped structure becomes larger.

- (3) The scale of the EMR particles is in the order of micrometers, and no obvious EMR particles are observed in the scale of nanometers, which indicates that the high-speed shear of the emulsifier makes the EMR evenly spread in the asphalt mortar at high temperatures. In addition, the EMR can react with the asphalt components to form a polymer with stable properties; the inclusion phase of the MRMA disappears, and the asphaltene and long-chain alkane in the mortar disappeared. The surface of the wax crystal adsorbs the polar groups in the asphaltene and the slurry, and the polar groups continue to form a double electric layer with the nearby asphaltene and the slurry. The directional dipole molecules of the double electric layer make the solvation layer wrap around the wax crystal. The inclusion phase consists of eutectic, polar micelle, and solvate layers. When the solvate layers are close to each other, there will be repulsive forces, so the inclusions do not cross each other. The EMR increases the concentration of the ionic compounds in asphalt mortar, and the ionic bond destroys the eutectic effect of the long-chain alkanes and wax crystal, causing the inclusion phase to disappear.

3.4.2. Force Displacement Curve. The microcosmic adhesion force (F_{ad}) is composed of van der Waals force (F_{vdw}), capillary force (F_c), electrostatic force (F_E), and chemical bond (F_B) and is characterized by the lowest point of the withdrawal curve. According to the AFM test process, the

asphalt sample and tip are all exposed to normal temperature air for quite a long time, so F_E is zero; the silicon nitride probe does not react with asphalt, so F_B is zero; the capillary force plays a role in promoting contact during the contact process and hindering separation during the withdrawal process, and the main source of microadhesion between the objects in the air is the capillary force, which is composed of hair fine action and liquid bridges. The force displacement curves of the MRMA and MA are shown in Figure 7.

- (1) Adhesion contact hysteresis: the ideal contact withdrawal path of rigid contact should be coincident, but Figure 7 shows that the force displacement path of the probe approaching and withdrawing from the asphalt sample surface is not the same; the approach path is A-B-C-D-E, and the withdrawal path is E-F-G-H-I, which is the phenomenon of adhesion contact lag, which generally exists in the microinterface. The phenomenon of adhesion contact hysteresis leads to the work required to separate the contact interface being greater than the work required to combine them, which leads to the withdrawal curve enveloping the approach curve.
- (2) Contact process: the microcosmic adhesion force (F_{ad}) between asphalt and the tip changes as the probe moves down and up, and the mechanical response of the microcantilever changes accordingly. When the probe goes down to the BD section, the resultant force at the cantilever end of the BD section includes van der Waals forces and capillary forces. van der Waals forces show attraction, and the capillary force and attraction are superposed in the same direction. At this time, the resultant force at the free end of the probe microcantilever is downward, the upper end of the cantilever is under tension, the lower end is under pressure, and the tension (pressure) force increases first and then decreases. When the probe goes down to the DE section, F_{ad} is the superposition of the van der Waals force and capillary force, and the overall performance is the repulsion force. At this time, the upper end of the microcantilever beam is under pressure, and the lower end is under tension; when the probe tip of point E contacts the asphalt surface, the probe stops going down after receiving the peak force.
- (3) Withdrawal process: when the probe is withdrawn to the EF section, the repulsion, attraction, and capillary forces are superposed in different directions, and the repulsion force decreases sharply as a whole; when the probe rises to the elevation corresponding to point F, the elevation corresponding to point F is zero, and the elevation corresponding to point F is lower than that of point D because the capillary force prevents the two interfaces from separating. When the probe is withdrawn to the FH section, the capillary force that prevents separation increases the force required to separate the tip and the asphalt surface. During the lifting process, one end of the microcantilever is subject to the force of lifting and

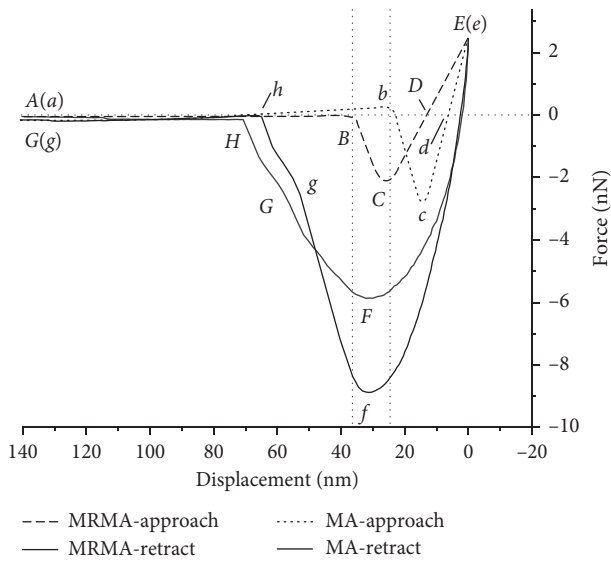


FIGURE 7: Force-displacement curve.

the other end is subject to the adhesion of F_{ad} , which causes the microcantilever to warp upward; at the G point, F_{ad} reaches the maximum value, and the separation distance between the interfaces is too large, which causes the capillary force to start to decrease; when the probe is lifted up to an elevation higher than that of the B point, the interface distance between the tip and asphalt is too large, and the van der Waals force is reduced to zero. At a certain point of BH, the liquid bridge forming between the tip of the needle and the asphalt breaks, and the capillary force disappears. This concludes a contact withdrawal cycle.

- (4) The function of a liquid bridge: both the probe exposed to air and the surface of asphalt form a liquid film. When the probe moves down to a certain position, a slit is formed between the tip of the needle and the asphalt surface, which has a very high adsorption potential; as the tip of the needle continues to move down, the slit gradually decreases, the adsorption potential gradually increases, and the free water molecules near the slit area are attracted to the slit area by the influence of the high adsorption potential of the slit area, resulting in condensation; finally, the tip of the needle punctures the water film on the asphalt surface and contacts the asphalt surface. The water molecular group extrudes into the slit area, and the capillary action makes the liquid film near the slit flow to the slit area. The high adsorption potential and extrusion and capillary co-accreration make the contact interface between the probe tip and asphalt form a liquid bridge. When the tip of the probe is separated from the asphalt, the width of the slit will reduce the adsorption potential, the gas-liquid interface of the liquid bridge will evaporate, the water molecule will escape, and the liquid bridge will dissipate; as the probe moves up,

the liquid bridge will be stretched and necked, the liquid bridge will gradually become thinner and longer until it finally breaks, leaving liquid masses on the tip of the probe and the asphalt surface. The fracture of the liquid bridge indicates that the probe tip is completely separated from the asphalt surface, which marks the end of a contact withdrawal cycle.

- (5) Difference between contact curves: the distance between the tip of the needle and the asphalt surface needed to produce attraction is called the attractive distance, which is expressed by D_a ; the height of the tip when the tip is completely separated from the asphalt surface is called the detached height, which is expressed by H_d . It can be seen from Figure 7 that, during the process of approaching, D_a (MRMA) $>$ D_a (MA), but the peak attraction of the asphalt to the tip of the needle is F (MRMA) $>$ F (MA). The CE segment is more moderate than the CE segment. The van der Waals force can only be induced by a pitch molecular group and probe tip molecular group within a certain distance. The elevation of the convex part of the bee-shaped MRMA structure is high, and the distribution is dense; thus, the probe tip can sense the van der Waals force at a higher height relative to that of the MA, and D_a (MRMA) $>$ D_a (MA) as the probe continues to move down. The attractive part and repulsive part of the van der Waals force change as the distance changes, and the liquid film collides on the asphalt surface at C (c). The viscosity of a liquid film with a micro- or nanoscale thickness is 4~8 orders of magnitude higher than that of bulk water (at 25°C, the viscosity of water is approximately 1 MPa s and the viscosity of asphalt is approximately 2.3×10^{11} MPa s), and the smaller the thickness is, the greater the viscosity is. When the probe is hit by the viscous resistance of the highly viscous liquid film and the repulsive force on the asphalt surface, the forward resistance of the probe increases gradually, and the force displacement curve turns at C (c); meanwhile, the CE (CE) segment does not obviously turn or jump. Therefore, it is considered that the thickness of the liquid film is the abscissa corresponding to the point C (c). The thickness of the liquid film of the MRMA is $X_C = 26.5$ nm and that of the MA is $X_C = 14.1$ nm. $X_C >$ X_C , indicating that the viscosity of the MRMA film is lower than that of the MA, which is the reason why the CE segment is more moderate than the CE segment. Due to the influence of the EMR, the number of honeycombs on the surface of the MRMA increases, the rough porous honeycombs have a higher adsorption potential than the smooth honeycombs, which is more conducive to the aggregation of water molecules, and the thickness of the liquid film on the surface of the MRMA increases. Therefore, the peak value of attraction during the process of exposure is $F_{MRMA} >$ F_{MA} . As the probe penetrates into the liquid film, the viscous resistance becomes larger, and the van der Waals

force changes from an attractive force to a repulsive force. The viscous resistance and van der Waals repulsive force are superposed, so the repulsive force sensed by the tip of the probe increases until it reaches the peak force.

- (6) Differences in the withdrawal curves: during the process of withdrawal, the peak value of the adsorption force of the asphalt on the tip of the needle is $F_{MRMA} < F_{MA}$, that is to say that $F_{ad}(MRMA) < F_{ad}(MA)$, $H_d(MRMA) > H_d(MA)$, the GH segment is nearly parallel to the GH segment, the abscissa is $x_F < x_B$, and $x_f > x_b$. The abscissa of point F is between B and C , indicating that when the MRMA produces the maximum adhesion force, $F_{ad}(MRMA)$ includes the van der Waals force and the capillary force; the abscissa of point F is behind point B , indicating that when the maximum adhesion force is generated, there is no van der Waals force between the tip of the needle and the asphalt, and the adhesion force at this time is mainly composed of the capillary force. The thin liquid film of the MA has a high viscosity and a greater adhesion to the tip than that of the MRMA, and there is a long chain of oil molecules adhering to the tip, resulting in $F_{ad}(MRMA) < F_{ad}(MA)$. The GH segment is nearly parallel to the GH segment, indicating that during the later stage of the contact withdrawal cycle, the stress of the probe is the same as that of the MRMA and MA, the liquid bridge neck shrinks to the fracture, and the tip of the probe disengages from the adhesion interface; as the probe continues to lift up, the liquid bridge is stretched to the necking state, and finally, the liquid bridge breaks at h and H points.

3.4.3. Surface Energy and Dissipation Energy. The surface energy and dissipation energy of the MRMA and MA were calculated by the adhesion contact theory combined with the force displacement curve produced by AFM to explore the micromodification mechanism of the EMR from the point of view of work and energy [16, 17].

After the force displacement curve is obtained, we need to analyze the data, so we need to choose an appropriate theoretical model. There are many commonly used theories, but the JKR theory is suitable for high adhesion systems; in addition, the rigid requirement of the object is low. Johnson, Kendall, and Roberts use the surface energy theory to modify the Hertz theory and obtain the JKR contact mechanics model [18]. Based on this model, the relationship between adhesion and the adhesion work is as follows:

$$F = \frac{3}{2}\pi RW, \quad (1)$$

where R is the equivalent radius of the curvature of the probe tip and W is the adhesion work.

The JKR model realizes the transformation from adhesion to adhesion work, and then, according to the principle of work energy transformation [19, 20], the transformation from adhesion work to surface energy is based on the

Fowkes model. The transformation relationship is shown in formulae (2) and (3):

$$\gamma_{ab} = \gamma_a + \gamma_b - 2\sqrt{\gamma_a^d \gamma_b^d}, \quad (2)$$

$$W_{ab} = 2\sqrt{\gamma_a^d \gamma_b^d}, \quad (3)$$

where γ_{ab} is interface energy; γ^d is dispersion component of the surface energy; and W_{ab} is adhesion work between interfaces.

For materials composed of nonpolar hydrocarbons, the dispersion component plays an absolutely dominant role in the surface energy component, so $\gamma_a \approx \gamma_a^d$. The expression of adhesion work can be approximately treated as follows:

$$W_{ab} = 2\sqrt{\gamma_a \gamma_b}. \quad (4)$$

It can be seen from formula (4) that, in the case of obtaining the probe surface energy γ_b , combined with the adhesion work between the probe and asphalt surface, the surface energy γ_a of asphalt can be calculated. According to the parameters provided by the manufacturer, the equivalent radius of the curvature of the probe is 20 nm, and the surface energy parameter is 1389.99 mJ/m². The calculation results of the asphalt adhesion work and surface energy are shown in Table 7.

According to the data in Table 7, the following analysis can be performed:

- (1) The surface microadhesion of the MRMA is only 62% that of the MA. At the same time and at the same temperature, the wax is more stable than the oil, and the wax crystal causes the free radicals of the molecular chain to cross each other and form clusters; meanwhile, the long chain molecules of the oil can produce displacement and adhesion under the external load; at the same time and at the position where maximum adhesion occurs, the viscous resistance of the membrane prevents the tip from leaving the asphalt surface. Therefore, the MA is more sensitive than the MRMA to the contact of the needle tip, has stronger attraction forces, and shows greater surface adhesion. It is proved that the bee structure is the structure formed by the development of a wax nodule center, and its component is a wax component. Waxy crystallization can increase the brittleness of asphalt and lead to the decrease in adhesion. The waxy crystallization of the MRMA to the surface of asphalt results in a slight decrease in the surface low-temperature crack resistance and an increase in the internal adhesion.
- (2) The surface energy of the MRMA is 45% that of the MA. The increase in the asphaltene content will lead to the decrease in the surface energy; in addition, the oxidation condensation of the EMR will lead to the increase in the asphaltene content in the MRMA system, so the surface energy of the MRMA will decrease but will decrease to a lower energy than that of the MA. The decrease in the surface energy of the

TABLE 7: The calculation results of the asphalt adhesion work and surface energy.

Species of asphalt	Adhesion (nN)	Interfacial energy ($\text{mJ} \cdot \text{m}^{-2}$)	Adhesive work ($\text{mJ} \cdot \text{m}^{-2}$)
MRMA	5.70	0.66	60.48
MA	9.18	1.47	97.40

MRMA shows that compared with the MA, the MRMA and other substances consume less energy to form surfaces, and it is easier to form a new surface; the decrease in the surface energy of the MRMA also shows that the MRMA is easier than the MA to disperse, which is conducive to the emulsification of asphalt. The theory of solid physics points out that the surface of an object with a high surface energy is in a high energy state, and the surface of the system is unstable; thus, the surface energy is reduced through the adsorption of other substances and surface polymerization to ensure the thermodynamic stability of the system. A high surface energy is one of the reasons why the adhesion force of the MA is greater than that of the MRMA. To reduce the surface energy of the MA system, the adsorption of the probe tip is more obvious, which shows that the MA system is more unstable than the MRMA system. Therefore, the stability of the MRMA is better than that of the MA.

- (3) The results show that the adhesive work of the MRMA is 62% that of the MA. The MA has a higher surface energy than the MRMA, and a surface with a high surface energy tends to reduce its surface energy. High energy surfaces will absorb more dissipative energy to reduce the surface energy, causing more surface damage and plastic deformation. The MRMA has a higher surface stiffness than the MA, which will convert more external force into elastic potential energy and will release it during the withdrawal stage so that the part of external force that is converted into dissipation energy will be reduced; meanwhile, it is more difficult for a wax surface than an oil surface to produce interfacial damage and plastic deformation, so the MRMA has a lower sensitivity than the MA to external force energy. Therefore, the dissipation energy of the MRMA is lower than that of the MA. During a contact withdrawal cycle, the MA receives more dissipated energy than the MRMA. Under cyclic loading, more damage is accumulated quickly in the microstructure of the MA than in that of the MRMA; in addition, damage develops more rapidly toward the direction of structural failure, so it is easier to produce fatigue damage in the MA than in the MRMA.

4. Conclusion

Powder:oil ratios of 0%, 3%, 6%, 9%, 12%, and 15% of the EMR with a particle size of approximately $35 \mu\text{m}$ were mixed into the matrix asphalt. To compare the modification effect of the different powder:oil ratios, the penetration test, softening point test, and ductility test were carried out. At

the same time, by also performing an X-ray diffraction test, an infrared spectrum analysis, an atomic force microscope analysis, and a differential scanning calorimetry analysis, the modification effect and mechanism of the EMR micro-powder asphalt were explored:

- (1) After grinding, the crystallinity of the EMR particles decreased, and at the same time, amorphous substances were produced, the specific surface area of the powder increased, and the activity of the powder increased.
- (2) The high-temperature performance of the asphalt improved, and the temperature sensitivity of the asphalt reduced after the EMR was added. However, the low-temperature performance of the asphalt was not significantly improved. The comprehensive performance of the asphalt was the best when the powder:oil ratio was 9%.
- (3) The N, P, S, and other atoms in the EMR formed weak hydrogen bond with the atoms in the asphalt, which did not share the electron pair, so the activity of the asphalt was enhanced. At the same time, the Al_2O_3 in the EMR adsorbed the small and medium molecular components of aliphatic hydrocarbons and aromatic hydrocarbons for oxidation, cross-linking, and condensation reactions at high temperatures. When the high molecular weight increased, the unreacted part of Al_2O_3 was replaced by the low molecular weight part and continued to play the role of the catalytic oxidant and increased the content of the high molecular weight hydrocarbon in the asphalt component to improve the performance of the matrix asphalt.
- (4) The compatibility between the EMR and asphalt is good, so it is more suitable to describe the micro-adhesion contact of asphalt materials with the JKR theory; a high surface energy will make asphalt absorb more dissipation energy, so the surface energy will decrease, resulting in the instability of the system; EMR can reduce the surface energy of the MRMA by increasing the asphaltene component, so the stability of the MRMA is better than that of the MA.

Data Availability

The datasets used and analyzed during the current study are available from the corresponding author on reasonable request.

Conflicts of Interest

The authors declare no conflicts of interest.

Acknowledgments

The research was supported by National Natural Science Foundation of China. (Grant no. 51768016) and Innovation Project of Guangxi Graduate Education, China (Grant no. YCSW2020043).

References

- [1] A. J. Brown, P. S. Francis, J. L. Adcock, K. F. Lim, and N. W. Barnett, "Manganese (III) and manganese (IV) as chemiluminescence reagents: a review," *Analytica Chimica Acta*, vol. 624, no. 2, pp. 175–183, 2008.
- [2] F. Han and L. Wu, *Industrial Solid Waste Recycling in Western China*, pp. 127–164, Springer, Singapore, 2019.
- [3] L. J. Y. Zhao and L. Zhou, "Improvement of bending fatigue test for asphalt surfacing on orthotropic steel bridge deck," *Advances in Civil Engineering Materials*, vol. 5, no. 1, pp. 325–336, 2016.
- [4] G. S. Kumar and S. N. Suresh, "Evaluation of workability and mechanical properties of nonfoaming warm mix asphalt mixtures," *Advances in Civil Engineering Materials*, vol. 7, no. 1, pp. 132–157, 2018.
- [5] B. Liu, Y. Zhang, M. Lu, Z. Su, G. Li, and T. Jiang, "Extraction and separation of manganese and iron from ferruginous manganese ores: a review," *Minerals Engineering*, vol. 131, pp. 286–303, 2019.
- [6] M. K. Sinha and W. Purcell, "Reducing agents in the leaching of manganese ores: a comprehensive review," *Hydrometallurgy*, vol. 187, pp. 168–186, 2019.
- [7] J. Lu, D. Dreisinger, and T. Glück, "Manganese electrodeposition—a literature review," *Hydrometallurgy*, vol. 141, pp. 105–116, 2014.
- [8] A. P. Das, L. B. Sukla, N. Pradhan, and S. Nayak, "Manganese biomining: a review," *Bioresource Technology*, vol. 102, no. 16, pp. 7381–7387, 2011.
- [9] B. Tang, S. Gao, Y. Wang, X. Liu, and N. Zhang, "Pore structure analysis of electrolytic manganese residue based permeable brick by using industrial CT," *Construction and Building Material*, vol. 208, pp. 697–709, 2019.
- [10] Y. Wang, S. Gao, X. Liu, B. Tang, E. Mukiza, and N. Zhang, "Preparation of non-sintered permeable bricks using electrolytic manganese residue: environmental and NH₃-N recovery benefits," *Journal of Hazardous Materials*, vol. 378, p. 120768, 2019.
- [11] C. Fang, R. Yu, S. Liu, and Y. Li, "Nanomaterials applied in asphalt modification: a review," *Journal of Materials Science & Technology*, vol. 29, no. 7, pp. 589–594, 2013.
- [12] Y. Zhang, X. Liu, Y. Xu, B. Tang, Y. Wang, and E. Mukiza, "Preparation and characterization of cement treated road base material utilizing electrolytic manganese residue," *Journal of Cleaner Production*, vol. 232, pp. 980–992, 2019.
- [13] P.-K. Hou, J.-S. Qian, Z. Wang, and C. Deng, "Production of quasi-sulfoaluminate cementitious materials with electrolytic manganese residue," *Cement and Concrete Composites*, vol. 34, no. 2, pp. 248–254, 2012.
- [14] F. Qin, Z. B. He, Q. N. Huang, and L. Q. Su, "Experiment study on the performance of manganese slag powder asphalt mixture," *Applied Mechanics and Materials*, vol. 71–78, pp. 3933–3937, 2011.
- [15] T. Zhou, L. Cao, E. H. Fini, L. Li, Z. Liu, and Z. Dong, "Behaviors of asphalt under certain aging levels and effects of rejuvenation," *Construction and Building Materials*, vol. 249, p. 118748, 2020.
- [16] I. Menapace, L. Garcia Cucalon, F. Kaseer et al., "Effect of recycling agents in recycled asphalt binders observed with microstructural and rheological tests," *Construction and Building Materials*, vol. 158, pp. 61–74, 2018.
- [17] D. Oldham, A. Hung, M. M. Parast, and E. H. Fini, "Investigating bitumen rejuvenation mechanisms using a coupled rheometry-morphology characterization approach," *Construction and Building Materials*, vol. 159, pp. 37–45, 2018.
- [18] K. L. Johnson and J. A. Greenwood, "An adhesion map for the contact of elastic spheres," *Journal of Colloid and Interface Science*, vol. 192, no. 2, pp. 326–333, 1997.
- [19] L. D. Poulidakos, S. D. Santos, M. Bueno, S. Kuentzel, M. Hugener, and M. N. Partl, "Influence of short and long term aging on chemical, microstructural and macro-mechanical properties of recycled asphalt mixtures," *Construction and Building Materials*, vol. 51, pp. 414–423, 2014.
- [20] M. Wang and L. Liu, "Investigation of microscale aging behavior of asphalt binders using atomic force microscopy," *Construction and Building Materials*, vol. 135, pp. 411–419, 2017.